Investigation of mechanical properties and thermal stability of the thinnest tungsten nanowire by density functional theory

Hui-Lung Chen[1], Shin-Pon Ju[2,3,*], Ken-Huang Lin[2], Jia-Yun Li[2], and Hsin-Tsung Chen[4]

[1] Department of Chemistry and Institute of Applied Chemistry, Chinese Culture University, Taipei, 111, Taiwan

[2] Department of Mechanical and Electro-Mechanical Engineering, National Sun Yat-sen University, Kaohsiung 804, Taiwan

[3]Department of Medicinal and Applied Chemistry, Kaohsiung Medical University, Kaohsiung 807, Taiwan

[4] Department of Chemistry, Chung Yuan Christian University, Taoyuan City 32023, Taiwan

Abstract

The most stable structure of the thinnest tungsten (W) nanowire with the radius of 1.9 Å was predicted by the simulated annealing basin-hopping method (SABH) with the tight-binding (TB) potential and the penalty algorithm. At this small scale, the predicted tungsten nanowire is helical instead of in the BCC arrangement found in bulk tungsten material. The density functional theory (DFT) calculation on the uniaxial tensile simulation was carried out to obtain the stress-strain profile of the thinnest tungsten nanowire. From the stress-strain curve, the Young's modulus is about 7.3% lower than that of bulk W, and the yielding stress is about 31 times higher than that of bulk W. The adsorption energy variations of an O_2 molecule on the top site of W atom at strain of 0 and 0.043 were used to explore the axial strain effect on the electronic properties of the thinnest W nanowire within the elastic region. Because the *d*-band center of the thinnest W nanowire at the strain of 0.043 becomes slightly closer to the Fermi level than that at strain of 0, the W atom of strained W nanowire becomes more reactive, resulting in the higher adsorption energy and the shorter W-O bond length. The density functional theory molecular dynamics (DFT-MD) simulation for the temperature elevation process was carried out for understanding the thermal stability of the thinnest W nanowire. The result shows the considerable deformation of local structure occurs at the temperature higher than 860K, indicating the thinnest W nanowire can be safely used at the temperature lower than 860K.

Keywords: Tungsten nanowire, simulated annealing basin-hopping, density functional theory, DFT-MD, mechanical property, and thermal stability.

Introduction

As the dimensions of materials decrease to several nanometers in size, the nature of their physical, chemical, and transport phenomena could be dramatically different from their bulk counterparts due to the surface effect, the small size effect, and the quantum effect [1-3]. Among all nanomaterials, one-dimensional nanostructures have been investigated widely both by empirical and theoretical approaches because they possess numerous new material properties superior to their bulk counterparts, such as higher mechanical strength [4, 5], lower electrical resistance [6, 7], higher thermal conductivity [8, 9], and better catalyst reactivity [10, 11]. These promising material properties also promote their applications in the nano-mechanical [12, 13] and nano-electronic devices [14], as well as high thermal conductivity materials and new catalysts.

Tungsten is a brittle metal which possesses higher tensile strength than those of most metal materials. Tungsten has great mechanical, chemical and electronic properties that allow for using in applications such as the single atom tip, gas molecule sensor, and electronic contact [15-17]. When bulk W is reduced to a one-dimensional W nanowire, its material properties are different from those of bulk W [18, 19]. For example, Huang [20] used the atomic force microscopy (AFM) to investigate the mechanical properties of one-dimensional tungsten nanowires along the axial direction. The experimental results showed that the average yield stress is about 8.44GPa, which is 1.67 to 2.48 times higher than that of bulk single crystal tungsten value (3.4 to 5.8GPa). Furthermore, the elastic modulus (270 GPa) is smaller than that of bulk tungsten (410 GPa) by about 140 GPa. Cimalla *et al.* [21] used AFM to study the mechanical properties of tungsten nanowires with diameters ranging from 100 nm to 300 nm by the bending experiments. The experimental results indicate that the Young's modulus is about 332GPa, which is very close to the bulk tungsten value of 355 GPa [22].

Other than the mechanical properties, the W nanowires also display other excellent electronic properties. W nanowires with diameters from 10 to 50 nm have been synthesized by Lee *et al.* [23], and they found the field enhancement factor is very close to the high efficient single-walled carbon nanotube emitters, something not seen in bulk W material. Yeong *et al*. investigated the field-emission properties of tungsten nanowire with 5 nm in diameter and several hundred nanometers in length [24]. The experimental results show that the high current density in field emitters leads to induced surface diffusion and crystallization of the disordered nanowire tip because the temperature rises at the field-emitting tip. In addition, Li *et al*. [25] used the FIB-CVD technique to grow ultra-thin and ultra-narrow tungsten lateral nanowires with widths and thicknesses comparable to the phase coherence length of bulk material, and determined that the wires are conductive and have a superconductive transition with a transition temperature (Tc) of about 5.1 K. According to these studies, the tungsten nanowires possess good electronic properties [12, 23, 26, 27] such that tungsten nanowires are worthy of investigation and synthesis as the one-dimensional nanomaterials.

Because it is very difficult to directly investigate the nanowire deformation at atomic scale during the related experiment, the powerful numerical method of molecular dynamics (MD) simulation was used to explore the atomic rearrangement of nanowires under external loading. Using this method, Peng *et al.* [28] investigated the deformation mechanism of Mo nanowires, and they found that both the orientation and lateral size have the significant effects on the deformation behaviours of Mo nanowires. In addition, Wang *et al.* [29] observed the uniaxial tensile strength of single-crystalline Mo nanowires, and the simulation results indicate that two phase transitions occur during the uniaxial tensile process. Furthermore, Li *et al.* [30] found that two kinds of structural transformation during stress deform polycrystalline Mo nanowires. One is the BCC configuration transforming into the intermediate configuration and then changing into FCC or HCP configuration. In another case, the FCC configuration converts into intermediate configuration and then changes into the BCC or HCP configuration. Using MD simulation, the mechanical behavior of the platinum nanowires was studied by Koh *et al.* [31]. Different strain rates of 0.04~0.4% ps^{-1} were employed to study the configuration changes under the tensile test. They found that the helical substructure was formed in the process of the tensile test at 300K. A similar result was also investigated in our previous study of helical gold nanowires [32].

In our previous study [33], the structure of the thinnest W nanowire was predicted by the simulated annealing basin-hopping method (SABH) with the penalty algorithm. Since studies of the mechanical properties and thermal stability of the thinnest W nanowire are still lacking both in empirical and theoretical approaches, the main objective of this study is to investigate the fracture mechanism and thermal stability of the thinnest W nanowire. The density functional theory (DFT) calculation was used to explore the deformation and fracture mechanism of the thinnest W nanowire by uniaxial tension, and its thermal stability was examined by the DFT-MD simulation during the temperature elevation process.

Simulation model

Fig. 1(a) and 1(b) show the unit cell, comprised of 44 atoms of the thinnest W nanowire, and the length of the unit cell along the axial direction is 27.9 Å after the optimization by the DFT calculation. The W nanowire was constructed by the SABH method with the tight-binding (TB) potential [34] and the penalty algorithm [35]. For the TB potential, the interaction between two W atoms depends not only on the distance between them, but also on their local environments. Moreover, the computing algorithm of TB potential is simpler than other many-body potentials. This model commences by summing the band energy, which is characterized by the second moment of the d-band density of state, and a pairwise potential energy of the Born-Mayer type and is expressed in the following form:

$$E_j = -\left\{\sum_j \xi^2 \, exp\left[-2q\left(\frac{r_{ij}}{r_0} - 1\right)\right]\right\}^{\frac{1}{2}} + \sum_j A exp\left[-p\left(\frac{r_{ij}}{r_0} - 1\right)\right] \quad (1)$$

where ξ is an effective hopping integral; r_{ij} is the distance between atom i and j; r_0 is the first-neighbour distance. The parameters of the TB potential relating to W are listed in Table 1. Furthermore, the interaction force on atom *i* is given by

$$\mathrm{F}_i = \sum_{j \neq i} \left\{\frac{\partial E_i}{\partial r_{ij}} + \frac{\partial E_j}{\partial r_{ij}}\right\} \quad (2)$$

In addition, the penalty function was adopted in the SABH method, which is used to constrain all atoms within a cylindrical space with a specific cross-section radius. The formula of the penalty method is shown as follows:

$$E_i^p = E_i + c \times p_i \begin{cases} c = 0, & x_i^2 + y_i^2 < r_0^2 \\ c = constant, & x_i^2 + y_i^2 \geq r_0^2 \end{cases} \quad (3)$$

$$p_i = [x_i^2 + y_i^2 - r_0^2]^2 \quad (4)$$

where E_i is the energy of atom *i* calculated by the TB potential, and p_i is the penalty potential. p_i is applied to atom *i* only if atom *i* is located outside the radius of nanowire (r_0), which was set for 2.5 Å in the current study. The terms x_i and y_i are the coordinates of atom *i* in x and y directions, and c is defined to discriminate whether the atom is in the wire radius range. The value c= 200 was adopted in this SABH calculation. In fact, c is independent of final structure as long as the c value is large enough. The formula of the penalty potential can be defined as any form which provides a constraint condition of the simulation model.

In Fig. 1(a) and 1(b), one can see that four W one-atom chains of two different colors are entangled, with a helical angle of 11.08° to form a helical W nanowire, designated as the H-wire. A closer observation, as in Fig. 1(c), reveals that atoms in the chains marked in blue form a relatively flat surface with their six first nearest neighbor atoms, and are designated as flat convex W atoms, W_f. The yellow atoms in the chains form a local sharp convex structure with their six first nearest atoms. Consequently, these atoms are labelled as sharp W convex atoms, W_s. Fig. 1(d) shows the cross section of the H-wire, and the distances between two W_s atoms (d_{ss}) of different chains and between two W_f atoms (d_{ff}), representing cross-sectional length, of different chains are 4.173 Å and 2.979 Å, respectively, indicating the cross section of H-wire is not circular.

For the tensile test, the strain was applied in the axial direction by increasing the periodic boundary length of 0.3Å after each DFT optimization process.

The normal strain in the axial direction ε is calculated as

$$\varepsilon = \frac{l_{z(t)} - l_{z(o)}}{l_{z(o)}} \tag{5}$$

where $l_{z(t)}$ is the unit cell length in the axial direction after conducting the tensile increment by t times, and $l_{z(o)}$ is its initial length at stress of 0. The uniaxial tensile stress of the nanowire structure was calculated according to the Nielsen-Martin scheme [36, 37], as the following equation [38] :

$$\sigma = \frac{1}{\Omega(\varepsilon)}\frac{\partial E}{\partial \varepsilon} \tag{6}$$

where the E is the total energy and Ω is the system volume at a given tensile strain of ε.

All DFT geometry optimizations and electronic property analyses were conducted by the $DMol^3$ package [39, 40]. The $DMol^3$ package settings employed DFT semi-core pseudo-potential (DSPP) calculations with double numerical basis set polarization *d*-functional (DND), and the generalized approximation (GGA) [41] by Perdew−Burke−Ernzerhof parameterization (PBE) [42] correction by using $(1 \times 1 \times 6)$ Monkhorst−Pack mesh k-points. Spin-polarization was considered in our calculation, and the SCF convergent conditions of electronic and ionic steps were set as 10^{-6} Ha and 10^{-5} Ha for the energy change during the geometry optimization process. To ascertain whether the DFT calculations are appropriate for the tungsten material, the calculated lattice constant was compared to the experimental value of a BCC W unit cell. The DFT predicted lattice constant is about 3.165Å, which is in good agreement with the experimental values of about 3.160Å [26] and 3.250Å [43, 44]. Furthermore, the bond length, vibrational frequency, and dissociation energy of the tungsten dimer were also compared to the available experimental values by the same DFT setting, as listed in Table 2. One can see that the frequency and dissociation energy predicted by DFT calculations are very close to the experimental values [45, 46].

For the thermal stability observation, the temperature elevation process from 300 to 1500 K was conducted by the DFT-MD simulation. The system was equilibrated before applying the subsequent temperature increment, and the Nosé–Hoover method was adopted to ensure a constant system temperature during the simulation process.

Results and discussion

To understand the mechanical property and the deformation mechanism of the H-wire, the tensile test was carried out by DFT calculation. The stress-strain profile of the H-wire is shown in Fig. 2, and the elongation process can be classified into three stages according to this profile. For more clearly discussing the corresponding stress-strain profile, the strains labeled by **a**, **b**, **c**, **d**, **e**, and **f** in Fig. 2 are used to indicate strains at 0, 0.064, 0.193, 0.268, 0.376, and 0.419, respectively. The corresponding morphologies are also displayed in Figs. 3(a)-3(f), with the color indicating atomic local shear strain value. The atomic local shear strain η_i^{Mises} of an individual atom *i*, introduced by Shimizu *et. al.* [47], was used to monitor the local structural deformation relative to all its first neighbor atoms according to the local structure of atom *i* relative to all its first neighbor atoms at the strain of 0. The detailed definition of η_i^{Mises} can be found in reference [48] of this study and is therefore not introduced here. A large η_i^{Mises} value indicates atom *i* is under the significant local plastic and shear deformation whereas a small η_i^{Mises} value implies atom *i* undergoes a small amount of movement relative to all of its first neighbor atoms or atom *i* is under local elastic deformation relative to all its first neighbor atoms. For the reference structure for calculating η_i^{Mises}, the η_i^{Mises} values of all atoms are zero and all atoms shown in Fig. 3(a) are marked in blue according to the η_i^{Mises} scale bar.

In the first stage (labels **a** to **b** in Fig. 2), the stress increases linearly with slight fluctuation until yielding occurs at yielding strain of **b** (0.064). The Young's modulus can be determined from the results of the tensile test for the strain of 2%, using linear regression. The calculated Young's modulus is about 381 Gpa, which is lower than the Young's modulus for bulk W of about 411 GPa by 7.3%. For the yielding stress, the value of the H-wire is about 17.81 Gpa, which is 31 times higher than that of bulk W (yielding stress of bulk W is 0.551 GPa). In Fig. 3(b), one can see the η_i^{Mises} value of each W atom is still very small, indicating the structures at strains lower than 0.064 are located within the elastic region, within which all atoms are still marked in blue according to the η_i^{Mises} scale bar.

From strain of 0.064 to 0.193 (labels **b** to **c** in Fig. 2), the stress remains at a roughly stable value with the fluctuation when the strain increases. In the diagram of the η_i^{Mises} distribution shown in Fig. 3(c) for the strain of 0.193, the middle portion of

H-wire represents η_i^{Mises} values which remain low, indicating that the local structures of this portion are only slightly deformed. However, the circled portion with higher η_i^{Mises} values becomes seriously distorted. To clearly investigate the circled portion, the right panels of Figs. 3(a)-3(c) show the local structures with the corresponding bond lengths and bending angles. There are four bond types indicated: the d_{ss}, d_{ff}, $d_{Ws\text{-}Ws}$, and $d_{Wf\text{-}Ws}$. The definitions of d_{ss} and d_{ff} were presented in Fig. 1(d), and the distance between two W_s atoms (or two W_f atoms) of the same chain and the distance between the W_s atom and its nearest W_f atom are designated as $d_{Ws\text{-}Ws}$, and $d_{Wf\text{-}Ws}$, respectively. Two bending angles, W_s-W_f-W_s and W_f-W_f-W_s, were considered, and these angles can be seen in these panels. At strain of 0, W_s-W_f-W_s and W_f-W_f-W_s are ~65° and ~60°, respectively. When the strain increases from 0 to 0.193, the angle W_s-W_f-W_s becomes larger, whereas the angle W_f-W_f-W_s becomes smaller. In terms of bond length variations with increasing strain, the $d_{Wf\text{-}Ws}$ value is almost unchanged. The d_{ss} and d_{ff} distances become slightly shorter by 6.9% (3.910Å at strain=0.193 and 4.2 Å at strain=0) and 2.1% (2.889 Å at strain=0.193 and 2.951 Å at strain=0) at strain of 0.193, whereas the $d_{Ws\text{-}Ws}$ (2.779 Å at strain=0; 3.195 Å at strain=0.193) becomes longer than that at strain of 0 by 13%.

At the last stage of the tensile test, from strain 0.193 to 0.419 (labels **c** to **f** in Fig. 2), the stress increases considerably when the strain increases from strain **c** to **e**, and then the stress displays a prominent drop from 30.4 to 8.4 GPa from strain **e** to **f**. Figs. 3(d)-3(f) show the η_i^{Mises} distributions for these strains of 0.268, 0.376, and 0.419, respectively. The η_i^{Mises} value of each atom is relatively higher than those shown in Fig. 3(b) for the structure within the elastic region. This indicates all W atoms of the H-wire at these strains are under significant distortion, and all atoms in Figs. 3(d)-3(f) are marked in red according to the η_i^{Mises} scale bar.

At strain of 0.419 (label **f** in Fig. 2), the cross sections enclosed by the dashed circle shown in Fig. 3(f) were comprised by two W atoms instead of four W atoms for the perfect H-wire.

To indicate the local structural deformation of the H-wire during the tensile test process, the average W_s-W_f-W_s and W_f-W_f-W_s angles and the average d_{ss}, d_{ff}, $d_{Ws\text{-}Ws}$, and $d_{Wf\text{-}Ws}$ distances are shown in Figs. 4(a) and 4(b). In Fig. 4(a), it is apparent that the W_s-W_f-W_s angle increases linearly with the increasing strain, whereas the W_f-W_f-W_s angle decreases linearly with the increasing strain. In terms of bond length variations in Fig. 4(b), the same labels **b** and **c** used in Fig. 2 are also adopted, and the inset of Fig. 4(b) shows the $d_{Wf\text{-}Ws}$ variation at a smaller vertical axial scale. From strain 0 to strain 0.064 (strain **b**), the $d_{Wf\text{-}Ws}$ value remains at a constant value of about 2.614 Å and then becomes slightly shorter from strain 0.064 to 0.1. As the strain increases from 0.1 to 0.4, the $d_{Wf\text{-}Ws}$ value displays an increasing trend. Values of d_{ss} and d_{ff} become slightly shorter when strain increases from 0 to 0.193, indicating the cross section of the H-wire becomes narrower by the tension load. However, the d_{ss} and d_{ff} distances remain almost unchanged after the strains are larger than 0.193. For $d_{Ws\text{-}Ws,}$ it is clear that this value monotonically increases with the tensile strain through the whole tension process.

The influence of tensile strain on the electroinc properties of the H-wire was investigated by the distributions of charge density difference for strains at 0, 0.064, and 0.193, as shown in Figs. 5(a)-5(c). The charge density difference is defined as the electron density distribution of the H-wire minus the electron density distributions of isolated W atoms which constitute this H-wire. In the left panels of Fig. 5, the iso-surfaces of charge accumulation at the iso-value of 0.05e are shown, while the charge depletion iso-surfaces at the iso-value of -0.005e are shown in the right panels of Fig.5. The distribution of positive iso-value between the W atoms indicates that extra electron accumulates between the W atoms after the W atoms form the H-wire at a strain of 0. For the distribution of negative iso-value shown in the right panels of Fig. 5, it indicates the charge depletion mainly occurs around W atoms. As the strain increases from 0 to 0.193, the charge deformation density for the charge accumulation occurs between two $d_{Wf\text{-}Ws}$ bonds, as can be seen in the area surrounded by dashed circle in the left panel of Fig. 5(c). In contrast, the charge depletion is found around W_s atoms or W_f atoms, as the one indicated by the arrow in the right panel of Fig. 5(a). One can see the charge depletion surfaces become slightly broader when the strain increases. From these results, it implies the distribution of electron density significantly varies during the tensile process even though the local structural slightly changes.

In our previous study, the CO oxidation mechanism on a W_{10} nanocluster was investigated and the Eley-Rideal (ER) mechanism was proven to be the most preferential channel [49]. The adsorption of an O_2 molecule on the W atom is a essential configuration for the ER reaction. Here, the adsorption energies of an O_2 molecule on the top site of an H-wire at strains of 0 and 0.043 were observed in order to understand the influence of axial stress on the O_2 adsorption energy. The adsorption energy was calculated according to the following equation:

$$\Delta E_{\text{ads}} = E_{[\text{total}]} - (E_{[\text{H-wire}]} + E_{[O_2]}) \qquad (7)$$

In this equation, the $E_{[\text{total}]}$, $E_{[\text{H-wire}]}$, and $E_{[O2]}$ correspond to the electronic energies of the adsorbed O_2 on the H-wire, the H-wire, and gaseous O_2, respectively.

The Fukui function [50] was used to be the criterion for finding the most reactive adsorption sites for H-wire. Parr *et al.* stated that the atom with the largest value for the Fukui function is associated with the most reactive site [51]. They found that a site having a larger f_k^- value is a better electron donor, whereas one having a larger f_k^+ value is a better electron acceptor. The Fukui function $f(r)$ is defined either as the first derivative of the chemical potential with respect to the external potential V(r) at a constant number of electrons *N*, or as the first derivative of the electronic density $\rho(r)$ with respect to the number of electrons N at constant external potential V(r):

$$f(r) = \left[\frac{\delta u}{\delta V(r)}\right]_N = \left[\frac{\partial \rho(r)}{\partial N}\right]_V \quad (8)$$

Because $\rho(r)$ as a function of N has slope discontinuities, the three reaction indices for governing electrophilic attack, governing nucleophilic attack, and governing radical attack are provided as follows:

$$f^-(r) = \left[\frac{\partial \rho(r)}{\partial N}\right]_V \quad (9)$$

$$f^+(r) = \left[\frac{\partial \rho(r)}{\partial N}\right]_V \quad (10)$$

$$f^0(r) = 1/2[f^+(r) + f^-(r)] \quad (11)$$

Yang and Mortier [52] defined $f(r)$ in a condensed form; these condensed Fukui functions of an atom k in a molecule with *N* electrons are defined as Eqs. (12), (13), and (14):

$$f_k^+ = [q_k(N+1) - q_k(N)] \quad (12)$$

$$f_k^- = [q_k(N) - q_k(N-1)] \quad (13)$$

$$f_k^0 = 1/2[q_k(N+1) - q_k(N-1)] \quad (14)$$

in which f_k^+, f_k^-, and f_k^0 represent nucleophilic, electrophilic, and radical attack, respectively; q_k is the electronic population of atom *k* in a molecule. Gázquez *et al.* [53] stated that the largest value of the Fukui function is, in general, associated with the most reactive site. According to the Fukui function analysis, when O_2 is adsorbed on the W surface, this molecule is the electronic acceptor and the distribution of f_k^- should be considered. Therefore, the distribution of Fukui function (f_k^-) is shown in Fig. 6 for determining different adsorption sites on the H-wire surface. In the current study, the f_k^- values were computed by using the Hirshfeld charge according to the Yang and Mortier method as demonstrated in Eq. (13). In Fig. 6, the W atoms marked in red (sharp convex atoms) have the larger f_k^- values, indicating these sites have higher activity than those marked in blue (flat convex atoms). During the tensile process within the elastic region, the distributions of Fukui function (f_k^-) are very similar, so the top site of one sharp convex atom was used to investigate the influence of tensile strain on the electroinc properties of the H-wire for O_2 adsorption.

The optimized configurations and the adsorption energies for the H-wire at strains of 0 and 0.043 are shown in Table 3. The bond length between O and W atoms for the H-wire at strain of 0.043 is shorter than that at strain of 0 by 13.4%, resulting in a 5.6% lower adsorption energy than that at strain of 0.

In order to further demonstrate the strain effect on the electronic structures of the H-wire, Figs. 7(a) and 7(b) show the partial electron density of states (PDOS) profiles of the W atom attaching to the O_2 molecule and the O atom of the O_2 molecule adsorbed by the W atom at strains of 0 and 0.043. The upper panels show the W atom PDOSs of *s*, *p*, and *d* orbitals, and lower panels display the O atom PDOSs of *s*, *p*, and *d* orbitals. At strain of 0, it can be seen that the W *p* orbital contributes more to the total DOS of occupied states near the Fermi level. At strain of 0.043, the PDOS of the W *d*-orbital between 0 and -4.0 eV at strain of 0 becomes slightly narrower and displays a slight right-shift. The PDOS peak of W *d*-orbital at -1.13 eV becomes broader and also displays a slight right-shift at strain of 0.043. With regards to the *d*-band center, the value at strain of 0 is -0.684 eV, while the value at strain of 0.043 becomes slightly closer to the Fermi level with a value of -0.672 eV, indicating the W atom becomes more reactive at the higher axial strain within the elastic region. As shown in Fig. 7(b), the PDOS of *p* and *d* orbitals of the O atom near the Fermi level becomes narrow and shifts toward the Fermi level, as indicated by the arrow.

In order to ensure the feasibility of the H-wire in nano-device applications, an examination of its thermal stability is necessary. Fig. 8 shows the relative energy of the H-wire at 300 K as temperature increases, drawn from DFT-MD simulation in the canonical ensemble (NVT). To indicate the temperature at which the H-wire undergoes a serious structural deformation, a parameter, ΔR, was used, and is defined as:

$$\Delta R = \sum_{i=1}^{n} \sum_{\substack{j=1 \\ i \neq j}}^{n} (r_{ij}), \text{ and } r_{ij} \leq r_{cut} \quad (15)$$

where r_{ij} is the distance between atoms i and j, and n is the total number of atoms. The value of r_{cut} is the half of the box length in the axial direction. The variation of this parameter is very sensitive to the structural change and any distinct increase or decrease in ΔR indicates the structure is undergoing a considerable deformation. In Fig. 8, both the relative energy and ΔR fluctuate at constant average values at temperatures ranging from 300 to 450 K, indicating the H-wire undergoes thermal vibration without any structural damage within this temperature range. When the temperature increases from 450 to 860 K, the relative energy begins to significantly decrease while ΔR increases. At 860 K, the relative energy is discontinuous and ΔR significantly increases as the temperature increases from 860 K, indicating the H-wire begins to undergo structural damage at 860 K. This finding implies that the H-wire is still very stable at temperatures higher than room temperature and can be further considered for their potential use.

Conclusions

The tensile test of the thinnest W nanowire has been conducted by the DFT calculation to obtain the stress-strain profile. From the stress-strain curve of the thinnest W nanowire, it can be found the Young's modulus is about 7.3% lower than that of bulk W, while the yielding stress of the thinnest W nanowire is about 31 times higher than that of bulk W. Within the elastic region, the axial strain effect on the electronic properties of the thinnest W nanowire is also investigated by the adsorption energy variations of an O_2 molecule on the top site of W atom at strain of 0 and 0.043. The DOS profiles of the W *d*-orbital show a slight right shift to the Fermi level for the thinnest W nanowire at strain of 0.043, compared to that at strain of 0. Because the *d*-band center of the thinnest W nanowire at strain of 0.043 becomes slightly closer to the Fermi level than that at strain of 0, the W atom of the strained W nanowire becomes more reactive, resulting in the higher adsorption energy and the shorter W-O bond length.

To understand the stability of the thinnest W nanowire, the temperature elevation process has carried out by the DFT-MD simulation from 300 to 1500K. The result indicates the melting point is about 860K, which is much lower than that of bulk W. For the applications in industry and other heat-resistant elements, the DFT-MD results indicate the thinnest W nanowire can be safely used at the temperature lower than 860K.

Acknowledgement

Authors would like to thank the Ministry of Science and Technology of Taiwan for their funding under the grant MOST101-2221-E-110-100-MY3, and are also grateful for the computational time, resources, and facilities of the National Center for High-Performance Computing, Taiwan, and the support from the National Center for Theoretical Sciences, Taiwan.

References

[1] H. Huang, Y. Q. Wu, S. L. Wang, Y. H. He, J. Zou, B. Y. Huang*, et al.*, "Mechanical properties of single crystal tungsten microwhiskers characterized by nanoindentation," *Materials Science and Engineering: A,* vol. 523, pp. 193-198, 2009.

[2] P. Villain, P. Beauchamp, K. F. Badawi, P. Goudeau, and P. O. Renault, "Atomistic calculation of size effects on elastic coefficients in nanometre-sized tungsten layers and wires," *Scripta Materialia,* vol. 50, pp. 1247-1251, 2004.

[3] H. Liang, M. Upmanyu, and H. Huang, "Size-dependent elasticity of nanowires: Nonlinear effects," *Physical Review B,* vol. 71, 2005.

[4] K. Gall, J. Diao, and M. L. Dunn, "The Strength of Gold Nanowires," *Nano Letters,* vol. 4, pp. 2431-2436, 2004.

[5] Y.-S. Sohn, J. Park, G. Yoon, J. Song, S.-W. Jee, J.-H. Lee*, et al.*, "Mechanical Properties of Silicon Nanowires," *Nanoscale Research Letters,* vol. 5, pp. 211-216, 2010.

[6] Q. Huang, C. M. Lilley, M. Bode, and R. S. Divan, "Electrical Properties of Cu Nanowires," in *Nanotechnology, 2008. NANO'08. 8th IEEE Conference on*, 2008, pp. 549-552.

[7] H. Park, R. Beresford, R. Ha, H.-J. Choi, H. Shin, and J. Xu, "Evaluation of metal–nanowire electrical contacts by measuring contact end resistance," *Nanotechnology,* vol. 23, p. 245201, 2012.

[8] D. Li, Y. Wu, P. Kim, L. Shi, P. Yang, and A. Majumdar, "Thermal conductivity of individual silicon nanowires," *Applied Physics Letters,* vol. 83, pp. 2934-2936, 2003.

[9] G. S. Doerk, C. Carraro, and R. Maboudian, "Single Nanowire Thermal Conductivity Measurements by Raman Thermography," *ACS Nano,* vol. 4, pp. 4908-4914, 2010/08/24 2010.

[10] O. Lotty, S. Biswas, T. Ghoshal, C. Glynn, C. O' Dwyer, N. Petkov*, et al.*, "Containing the catalyst: diameter controlled Ge nanowire growth," *Journal of Materials Chemistry C,* vol. 1, pp. 4450-4456, 2013.

[11] B. H. Kim and J. W. Kwon, "Metal Catalyst for Low-Temperature Growth of Controlled Zinc Oxide Nanowires on Arbitrary Substrates," *Sci. Rep.,* vol. 4, 03/14/online 2014.

[12] V. Cimalla, C.-C. Röhlig, J. Pezoldt, M. Niebelschütz, O. Ambacher, K. Brückner*, et al.*, "Nanomechanics of Single Crystalline Tungsten Nanowires," *Journal of Nanomaterials,* vol. 2008, pp. 1-9, 2008.

[13] Y.-H. Wen, R. Huang, Z.-Z. Zhu, and Q. Wang, "Mechanical properties of platinum nanowires: An atomistic investigation on single-crystalline and

twinned structures," *Computational Materials Science,* vol. 55, pp. 205-210, 2012.

[14] K. S. Yeong and J. T. L. Thong, "Field-emission properties of ultrathin 5 nm tungsten nanowire," *Journal of Applied Physics,* vol. 100, p. 114325, 2006.

[15] A. Löfberg, L. Seyfried, P. Blehen, S. Decker, J. M. Bastin, and A. Frennet, "Pore structure of bulk tungsten carbide powder catalysts," *Catalysis Letters,* vol. 33, pp. 165-173, 1995.

[16] H. J. F. Jansen and A. J. Freeman, "Total-energy full-potential linearized augmented-plane-wave method for bulk solids: Electronic and structural properties of tungsten," *Physical Review B,* vol. 30, pp. 561-569, 07/15/ 1984.

[17] T. Hirai, E. Bondarchuk, A. I. Borovkov, T. Koppitz, J. Linke, P. Mertens*, et al.*, "Development and testing of a bulk tungsten tile for the JET divertor," *Physica Scripta,* vol. 2007, p. 144, 2007.

[18] Y.-C. Chou, K. Hillerich, J. Tersoff, M. C. Reuter, K. A. Dick, and F. M. Ross, "Atomic-Scale Variability and Control of III-V Nanowire Growth Kinetics," *Science,* vol. 343, pp. 281-284, January 17, 2014 2014.

[19] A. Yang, W. Fa, X. Li, and J. Dong, "Vibrational properties between silver (4,4) nanotube and nanowire," *Journal of Applied Physics,* vol. 110, pp. -, 2011.

[20] H. Huang, Y. Q. Wu, S. L. Wang, Y. H. He, J. Zou, B. Y. Huang*, et al.*, "Mechanical properties of single crystal tungsten microwhiskers characterized by nanoindentation," *Materials Science and Engineering a-Structural Materials Properties Microstructure and Processing,* vol. 523, pp. 193-198, Oct 2009.

[21] V. Cimalla, C. C. Rohlig, J. Pezoldt, M. Niebelschutz, O. Ambacher, K. Bruckner*, et al.*, "Nanomechanics of single crystalline tungsten nanowires," *Journal of Nanomaterials,* 2008.

[22] D. Mende and G. Simon, *Physik: Gleichungen und Tabellen*: Carl Hanser Verlag GmbH Co KG, 2013.

[23] Y.-H. Lee, C.-H. Choi, Y.-T. Jang, E.-K. Kim, B.-K. Ju, N.-K. Min*, et al.*, "Tungsten nanowires and their field electron emission properties," *Applied Physics Letters,* vol. 81, pp. 745-747, 2002.

[24] K. S. Yeong and J. T. L. Thong, "Field-emission properties of ultrathin 5nm tungsten nanowire," *Journal of Applied Physics,* vol. 100, pp. -, 2006.

[25] W. Li, J. C. Fenton, C. Gu, and P. A. Warburton, "Superconductivity of ultra-fine tungsten nanowires grown by focused-ion-beam direct-writing," *Microelectronic Engineering,* vol. 88, pp. 2636-2638, 2011.

[26] J.-Y. Kim, D. Jang, and J. R. Greer, "Tensile and compressive behavior of tungsten, molybdenum, tantalum and niobium at the nanoscale," *Acta Materialia,* vol. 58, pp. 2355-2363, 2010.

[27] S. Li, X. Ding, J. Li, X. Ren, J. Sun, and E. Ma, "High-Efficiency Mechanical Energy Storage and Retrieval Using Interfaces in Nanowires," *Nano Letters,* vol. 10, pp. 1774-1779, 2010.

[28] P. Wang, W. Chou, A. Nie, Y. Huang, H. Yao, and H. Wang, "Molecular dynamics simulation on deformation mechanisms in body-centered-cubic molybdenum nanowires," *Journal of Applied Physics,* vol. 110, p. 093521, 2011.

[29] J. Wang, W. Hu, X. Li, S. Xiao, and H. Deng, "Strain-driven phase transition of molybdenum nanowire under uniaxial tensile strain," *Computational Materials Science,* vol. 50, pp. 373-377, 12// 2010.

[30] X. Li, W. Hu, S. Xiao, and W.-Q. Huang, "Stress-induced phase transformation and strain rate effect in polycrystalline Mo nanowires," *Physica E: Low-dimensional Systems and Nanostructures,* vol. 43, pp. 1131-1139, 2011.

[31] S. J. A. Koh, H. P. Lee, C. Lu, and Q. H. Cheng, "Molecular dynamics simulation of a solid platinum nanowire under uniaxial tensile strain: Temperature and strain-rate effects," *Physical Review B,* vol. 72, p. 085414, 2005.

[32] S.-P. Ju, W.-J. Lee, J.-S. Lin, and M.-L. Liao, "Strain rate effect on tensile behavior of the helical multi-shell gold nanowires," *Materials Chemistry and Physics,* vol. 100, pp. 48-53, 2006.

[33] K.-H. Lin, J.-Y. Li, J.-S. Lin, S.-P. Ju, J.-M. Lu, and J.-Y. Hsieh, "Mechanical properties and thermal stability of ultrathin tungsten nanowires," *RSC Advances,* vol. 4, pp. 6985-6990, 2014.

[34] V. Rosato, M. Guillope, and B. Legrand, "Thermodynamical and structural properties of f.c.c. transition metals using a simple tight-binding model," *Philosophical Magazine A,* vol. 59, pp. 321-336, 1989.

[35] G. N. Vanderplaats, *Numerical optimization techniques for engineering design: with applications* vol. 1: McGraw-Hill New York, 1984.

[36] O. H. Nielsen and R. M. Martin, "Quantum-mechanical theory of stress and force," *Physical Review B,* vol. 32, pp. 3780-3791, 1985.

[37] O. H. Nielsen and R. M. Martin, "Erratum: Quantum-mechanical theory of stress and force," *Physical Review B,* vol. 35, pp. 9308-9308, 1987.

[38] Y.-L. Liu, H.-B. Zhou, Y. Zhang, S. Jin, and G.-H. Lu, "The ideal tensile strength and deformation behavior of a tungsten single crystal," *Nuclear Instruments and Methods in Physics Research Section B: Beam Interactions with Materials and Atoms,* vol. 267, pp. 3282-3285, 2009.

[39] B. Delley, "An all-electron numerical method for solving the local density functional for polyatomic molecules," *The Journal of chemical physics,* vol. 92, pp. 508-517, 1990.

[40] B. Delley, "From molecules to solids with the DMol3 approach," *The Journal of Chemical Physics,* vol. 113, pp. 7756-7764, 2000.

[41] D. C. Langreth and J. P. Perdew, "Theory of nonuniform electronic systems. I. Analysis of the gradient approximation and a generalization that works," *Physical Review B,* vol. 21, pp. 5469-5493, 1980.

[42] J. P. Perdew, K. Burke, and M. Ernzerhof, "Generalized Gradient Approximation Made Simple," *Physical Review Letters,* vol. 77, pp. 3865-3868, 1996.

[43] J. Du, X. Sun, D. Meng, P. Zhang, and G. Jiang, "Geometrical and electronic structures of small Wn(n=2–16) clusters," *The Journal of Chemical Physics,* vol. 131, p. 044313, 2009.

[44] M. J. Mehl and D. A. Papaconstantopoulos, "Applications of a tight-binding total-energy method for transition and noble metals: Elastic constants, vacancies, and surfaces of monatomic metals," *Physical Review B,* vol. 54, pp. 4519-4530, 1996.

[45] Z. Hu, J. G. Dong, J. R. Lombardi, and D. M. Lindsay, "Optical and Raman spectroscopy of mass-selected tungsten dimers in argon matrices," *The Journal of Chemical Physics,* vol. 97, pp. 8811-8812, 1992.

[46] M. D. Morse, "Clusters of transition-metal atoms," *Chemical Reviews,* vol. 86, pp. 1049-1109, 1986.

[47] F. Shimizu, S. Ogata, and J. Li, "Theory of shear banding in metallic glasses and molecular dynamics calculations," *Materials Transactions,* vol. 48, pp. 2923-2927, 2007.

[48] J. T. Wang, P. D. Hodgson, J. D. Zhang, W. Y. Yan, and C. H. Yang, "Effects of pores on shear bands in metallic glasses: A molecular dynamics study," *Computational Materials Science,* vol. 50, pp. 211-217, 2010.

[49] M. H. Weng and S. P. Ju, "CO Oxidation Mechanism on Tungsten Nanoparticle," *The Journal of Physical Chemistry C,* vol. 116, pp. 18803-18815, 2012.

[50] K. Fukui, "Role of Frontier Orbitals in Chemical Reactions," *Science,* vol. 218, pp. 747-754, November 19, 1982, 1982.

[51] R. G. Parr and W. Yang, "Density functional approach to the frontier-electron theory of chemical reactivity," *Journal of the American Chemical Society,* vol. 106, pp. 4049-4050, 1984.

[52] W. Yang and W. J. Mortier, "The use of global and local molecular parameters for the analysis of the gas-phase basicity of amines," *Journal of the American Chemical Society,* vol. 108, pp. 5708-5711, 1986.

[53] J. L. Gazquez and F. Mendez, "The Hard and Soft Acids and Bases Principle: An Atoms in Molecules Viewpoint," *The Journal of Physical Chemistry,* vol.

98, pp. 4591-4593, 1994.

Table1 The bulk tight-binding potential parameters

	A (eV)	ξ (eV)	p	q	r_0 (Å)
W	0.249	3.2055	10.3715	1.9916	2.741

Table 2 The tungsten dimer calculation results for the bond length, vibrational frequency, and binding energy using PBE functional for comparing with the available experiment results.

	Method	**R (Å)**	**ω(cm^{-1})**	**E_d(eV)**
W_2	PBE/DNP/DSPP	2.055[a]	317.3[a]	4.86[a]
	Exp.		337[b]	5 ±1[c]

[a]This work, [b]Reference [45], [c]Reference [46],

Table 3 Adsorption energies and the configurations of an O_2 molecule on the W nanowire at strains of 0 and 0.043. The length unit in the adsorption configurations is Å.

Strain	Adsorption energy (eV)	Configuration
0.0	-2.080	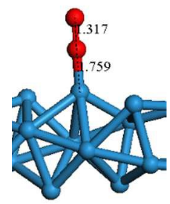
0.043	-2.196	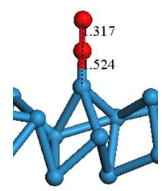

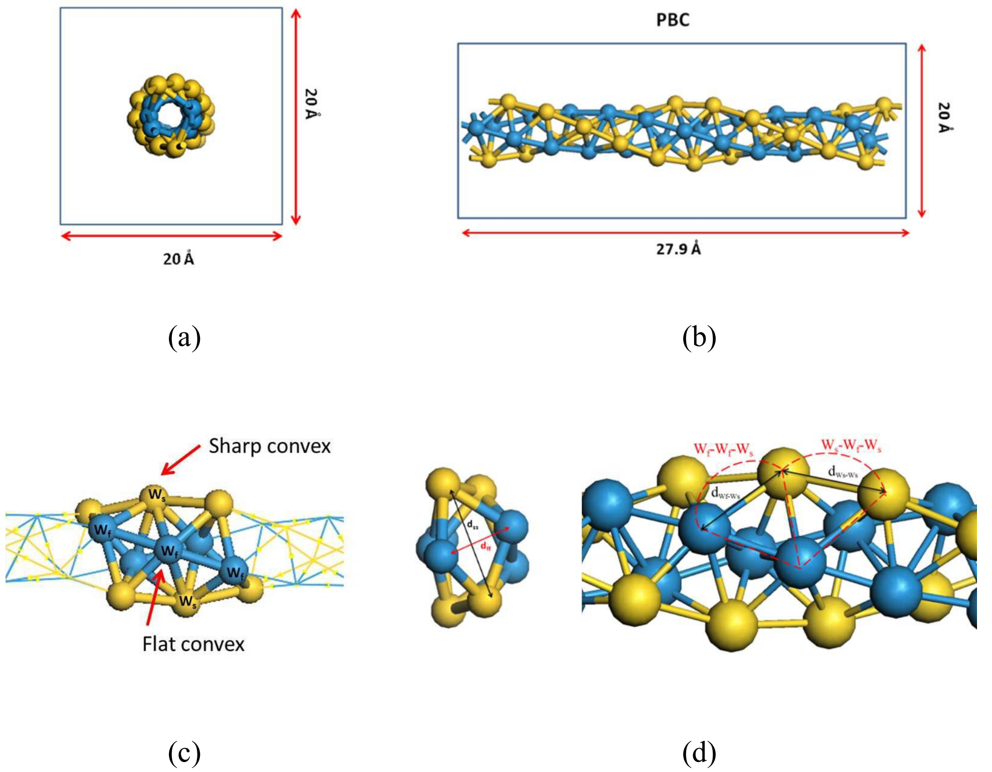

Figure 1 Schematic diagram of W helical nanowire (a) cross-sectional view, (b) side view, (c) local side view, and (d) the bond lengths d_{ss}, d_{ff}, $d_{Ws\text{-}Ws}$, and $d_{Wf\text{-}Ws}$ and two bending angles W_s-W_f-W_s and W_f-W_f-W_s.

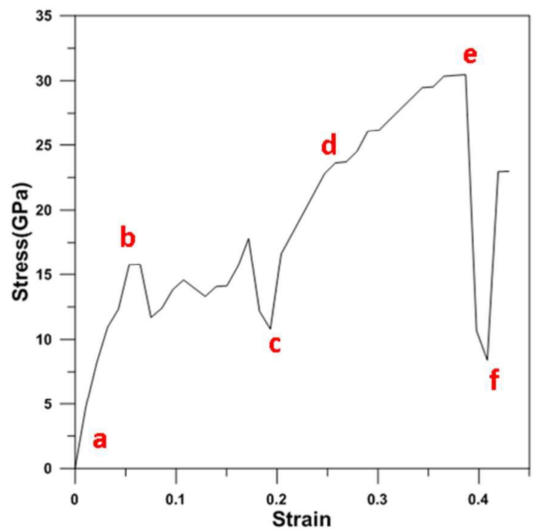

Figure 2 Stress-strain relationship for the W helical nanowire under the tensile test.

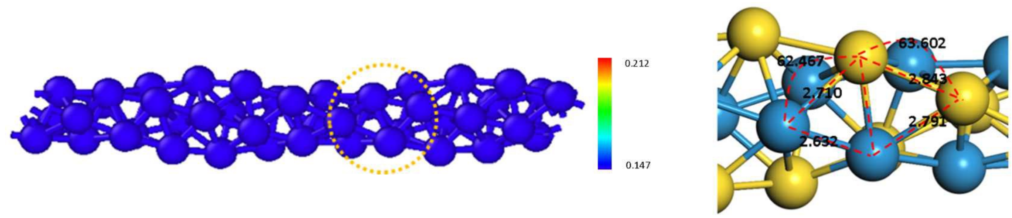

(a) strain = 0

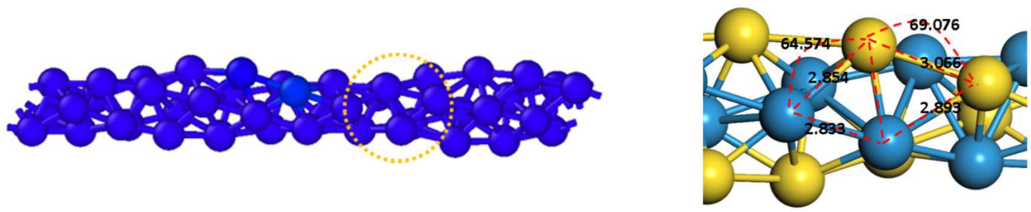

(b) strain = 0.064

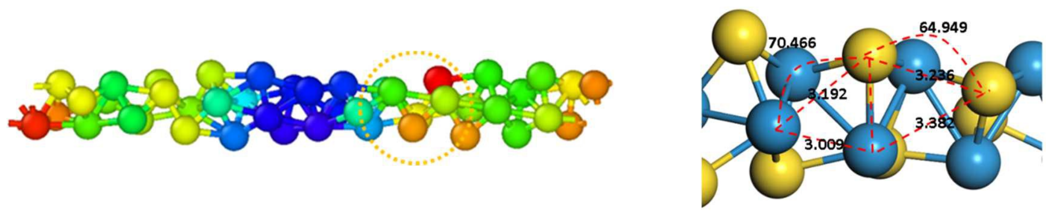

(c) strain = 0.193

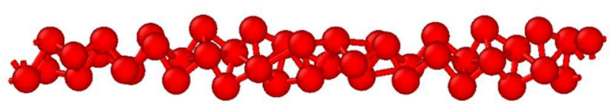

(d) strain = 0.268

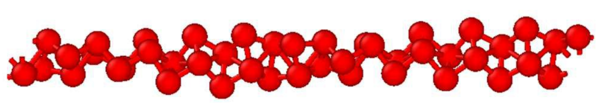

(e) strain = 0.376

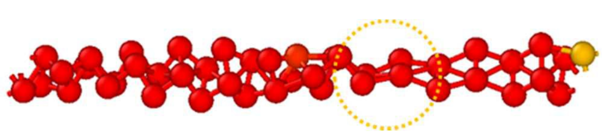

(f) strain = 0.419

Figure 3 Snapshots and local strain analysis of tensile process of the W helical nanowire at different strains. Atoms are colored according to their atomic shear strain η_i^{Mises} values. In the right panels of figures (a)-(c), the respective angles and bond lengthes are shown in units of degree and Å, respectively.

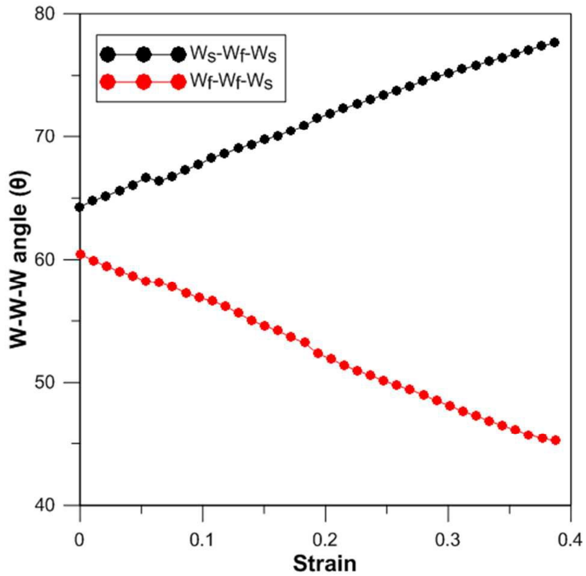

(a)

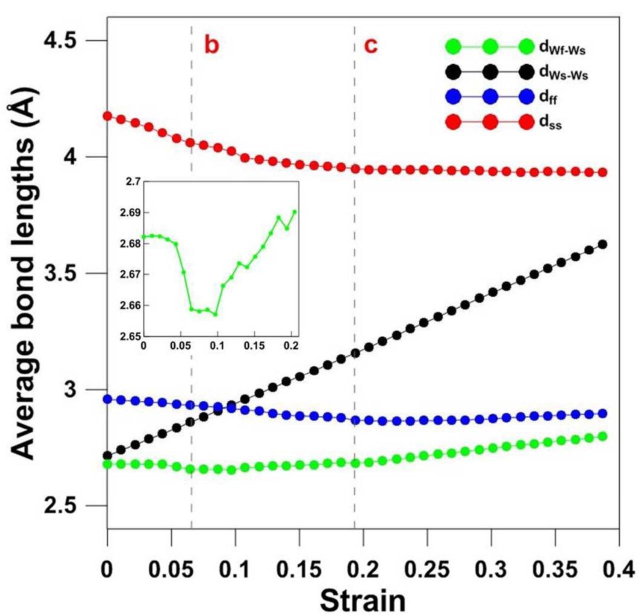

(b)

Figure 4 Local structural analysis of the W helical nanowire during the tensile process. (a)Average angles, and (b) average bond lengths. Inset is $d_{wf\text{-}ws}$ at local scale at strain from 0 to 0.2.

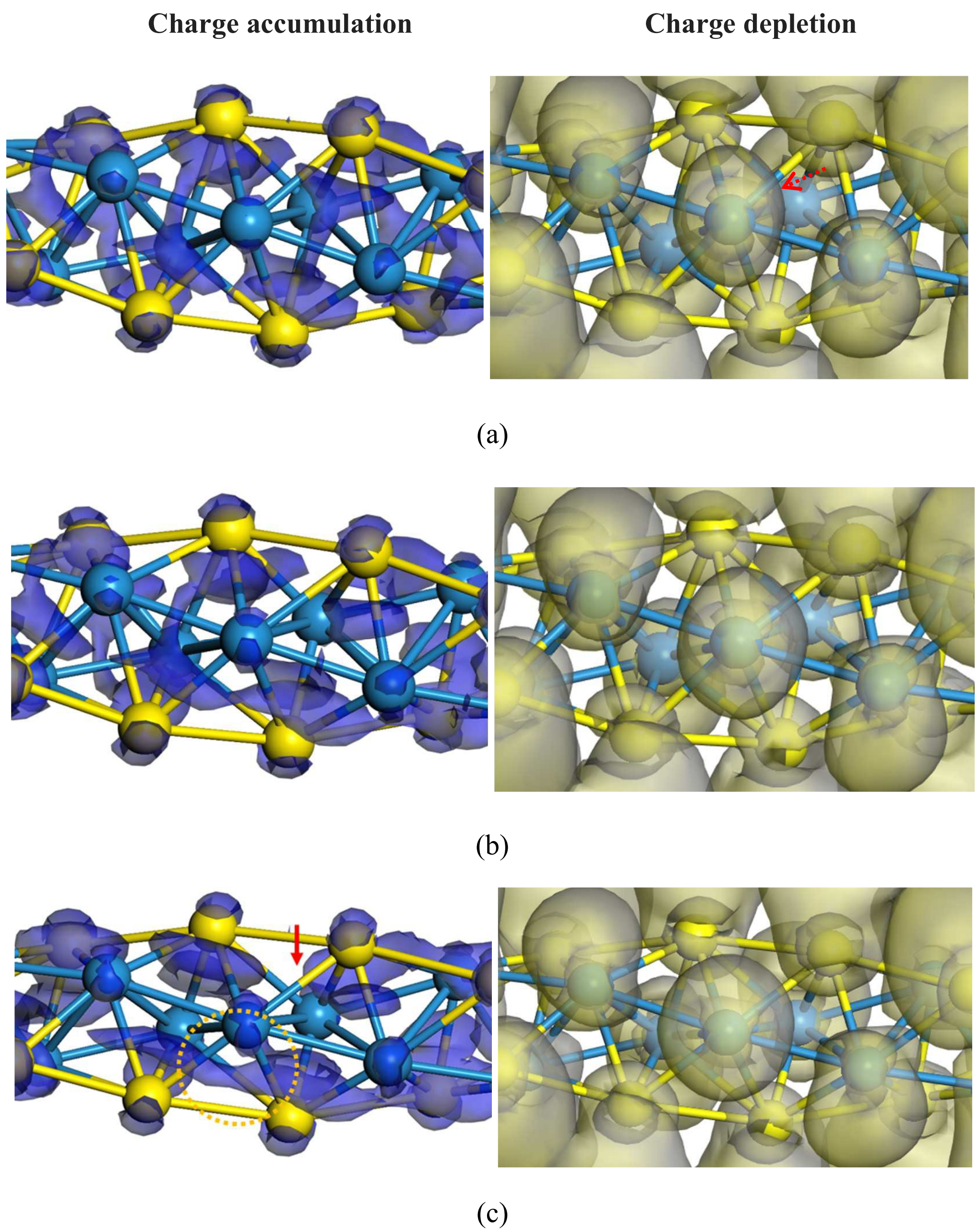

Figure 5 The charge density difference distributions of the helical W nanowire at different strains. The unit of charge density difference is the elementary charge (e). The iso-value used on the left panels is 0.05e for the charge accumulation, whereas the iso-value used on the right panels is -0.005e for the charge depletion. (a) Strain = 0, (b) strain = 0.064, (c) strain = 0.193. Circled and arrow areas indicate the distributions of charge density difference transfer depending on strain values.

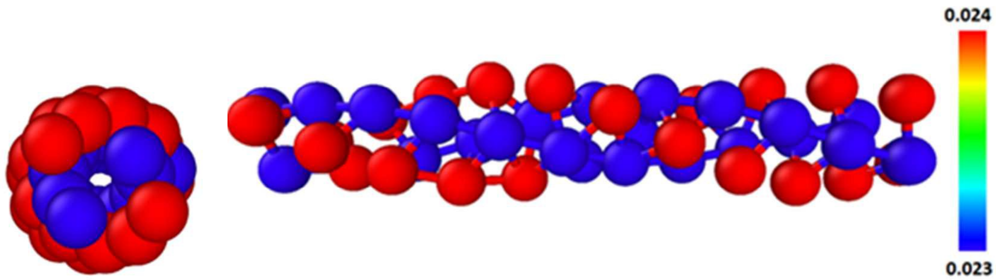

Figure 6 The f_k^- distribution on each atom of W helical nanowire: (right) side view; (left) cross-sectional view. Atoms are colored according to their f_k^- values and the unit of f_k^- value is the elementary charge (e).

Strain=0 Strain=0.043

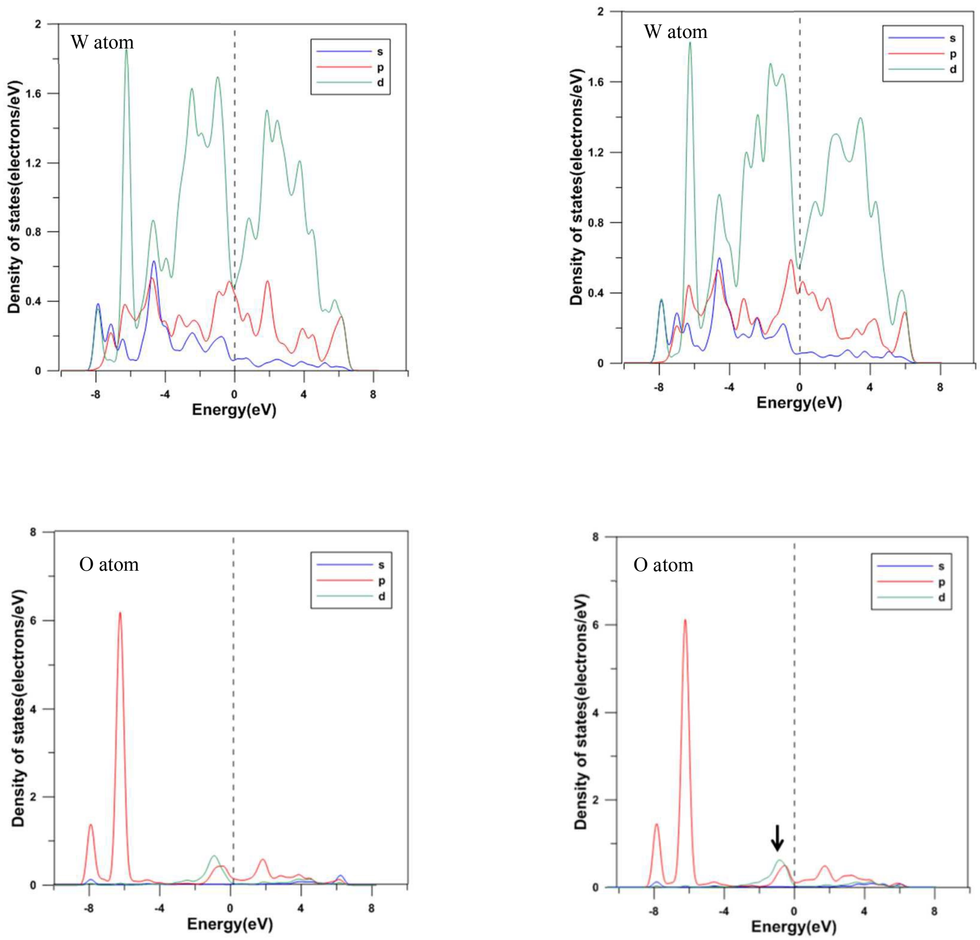

(a) (b)

Figure 7 Partial density of states (PDOSs) of W and O atoms of the W helical nanowire under tensile process at (a) Strain =0, and (b) strain=0.043. Upper panels are PDOS profiles of the W atom attaching to the O_2 molecule, and lower panels are the PDOS profiles of the O atom.

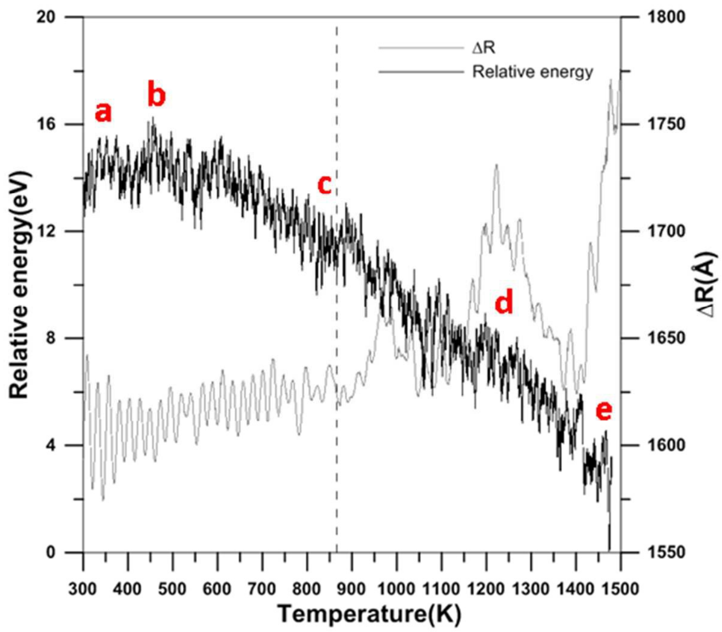

Figure 8 Variations in relative energy and ΔR during the temperature elevation process of the W helical nanowire.